European Conference on Computational Fluid Dynamics
ECCOMAS CFD 2006
P. Wesseling, E. Oñate, J. Périaux (Eds)

NUMERICAL SIMULATION OF SEPARATED FLOW OVER FLEXIBLE STRUCTURAL MEMBRANES

Lisa A. Matthews, Deborah M. Greaves and Chris J. K. Williams

Department of Architecture and Civil Engineering,
University of Bath, Bath, BA2 7AY, United Kingdom
e-mail: L.A.Matthews@bath.ac.uk

Key words: Finite Volume, incompressible, unstructured, non-orthogonal, moving boundary

Abstract. *This paper describes the formulation of a computational Fluid-Structure Interaction (FSI) algorithm for the solution of the unsteady flow of an incompressible fluid around a flexible structural membrane undergoing large deformations. A boundary fitted unstructured triangular mesh is used, and the Navier-Stokes equations are discretised using a collocated Finite Volume method with the SIMPLE algorithm for pressure solution. Initial test cases, both steady and unsteady, and on stationary and arbitrarily moving meshes give encouraging results in comparison with published experimental and numerical data.*

1 INTRODUCTION

Many fields of engineering design require an understanding of the interactions between fluids and flexible membrane-type structures, such as the design of sails, flags, parachutes, airbags and lightweight fabric building structures. Blood flow in heart valves and aneurysm formation, insect flight and swimming of aquatic invertebrates are some biological examples.

A challenge in the modelling of such systems is the flexible nature of the structure or membrane involved. Forces generated by the fluid flow induce large displacements and deformations of the structure due to its flexibility. This changes the fluid domain and fluid flow characteristics, in turn changing the forces and thus displacements of the structure. Realistic results from experimental testing of such systems are mostly very difficult to achieve due to the high flexibility of the structure and the very large deformations it undergoes.

Computational investigation into the motion of membrane airfoils and sails has been undertaken, for example, by Jackson and Christie[1] and Jackson and Fiddes[2] who use an inviscid vortex lattice method and a coupled inviscid-boundary layer model respectively. It is recognised that the accurate representation of the effects of viscosity, such as regions of separated flow, is essential in this case and potential flow models are therefore insufficient. To tackle this problem, Shyy and Smith[3] consider viscous flow past membrane wings using the finite volume method to discretise the Navier-Stokes equations on a body-fitted curvilinear structured grid, coupled to a finite difference model for the membrane dynamics. Viscous effects were found to dominate the behaviour of the system[4].

The motion of a one-dimensional structure moving in a two-dimensional fluid has recently been investigated by Farnell, David and Barton[5] considering the motion of flexible filaments flowing in soap films. A finite element formulation is used to discretise the Navier-Stokes equations, and the filament motion is modelled as an ‘N-tuple’ pendulum with hinge stiffness and damping, which moves across the stationary fluid mesh. Recirculation zones forming near the leading edge were found to interact strongly with the filament due to its flexibility. The vortices were convected down the length of the filament and finally shed from the trailing edge; the filament curvature was at the same time a cause of the separation and a result of the vortex itself, demonstrating the complexity of behaviour exhibited by this relatively simple system.

Stein *et al*[6] consider the behaviour of round parachutes and give reference to a number of previous studies. The Deforming-Spatial-Domain / Stabilised-Space-Time finite element approach is used which automatically takes into account the motion of the domain boundaries. When considering the interactions of a parachute with the far-wake of an aircraft[7] a multi domain method is used with the domain attached to the parachute moving over the domain containing the aircraft. The mesh is considered to be a linear elastic solid with imposed deformations at the fluid-canopy interface.

This research project aims to study such large displacement fluid-structure interaction (FSI) problems through the development of a computational FSI code. The Navier-Stokes equations describing the behaviour of a viscous Newtonian fluid are discretised on a moving unstructured triangular mesh using a collocated finite volume method. In two-dimensions the membrane structure is represented by a continuous array of one-dimensional line segments which are a subset of the fluid mesh edges, and is analysed considering the dynamic behaviour of the system. The fluid mesh remains attached to the membrane as it deforms, and the connectivity of the mesh remains constant throughout the simulation.

2 DISCRETISATION OF THE GOVERNING EQUATIONS

2.1 Computational mesh

An unstructured triangular body-fitted mesh is used. This allows complex shaped domains to be meshed in a relatively straightforward manner, with no special treatment of the mesh needed at the boundaries. All computational volumes have the same topology, which simplifies the data structure and computer code. An unstructured approach also allows mesh nodes to be concentrated in regions of interest easily and efficiently, such as in the boundary layer near a solid wall.

Here a Delaunay triangulation generator[8] is used to create initial mesh based on boundary geometry and discretisation. The minimum internal angle of the mesh is limited to 30°.

2.2 Equations of motion

The equations of motion describing the unsteady flow of an incompressible Newtonian fluid, in two dimensions are:

$$\rho \frac{\partial \mathbf{U}}{\partial t} = \mu \nabla \cdot \nabla \mathbf{U} - \rho \nabla \cdot \left(\mathbf{U}\mathbf{U} \right) - \nabla p \tag{1}$$

$$\nabla \cdot \mathbf{U} = 0 \tag{2}$$

where ρ is the density and μ is the dynamic viscosity of the fluid, $\mathbf{U}$ is the vector of fluid velocity, p is the pressure and t is time. Equation (1), in component, form is:

$$\rho\frac{\partial u}{\partial t} = \mu\nabla\cdot\nabla u - \rho\nabla\cdot\left(\mathbf{U}u\right) - \nabla p\cdot\mathbf{i} \tag{3a}$$

$$\rho\frac{\partial v}{\partial t} = \mu\nabla\cdot\nabla v - \rho\nabla\cdot\left(\mathbf{U}v\right) - \nabla p\cdot\mathbf{j} \tag{3b}$$

where u and v are the components of the velocity vector $\mathbf{U}$ in the x- and y- directions respectively, and $\mathbf{i}$ and $\mathbf{j}$ are the x- and y- direction base vectors respectively.

2.3 Discretisation

Using the unstructured triangular mesh as described previously, the collocated cell-centred approach is taken, wherein all three independent unknown variables (pressure and two components of velocity) are located at the centroid of the triangular control volume. Following the Finite Volume formulation, the equations of motion are integrated over the control volume surrounding the computational node P as shown in Figure 1. The equations will be discretised first on a stationary mesh, and then extended to the case of a moving mesh in section 2.10.

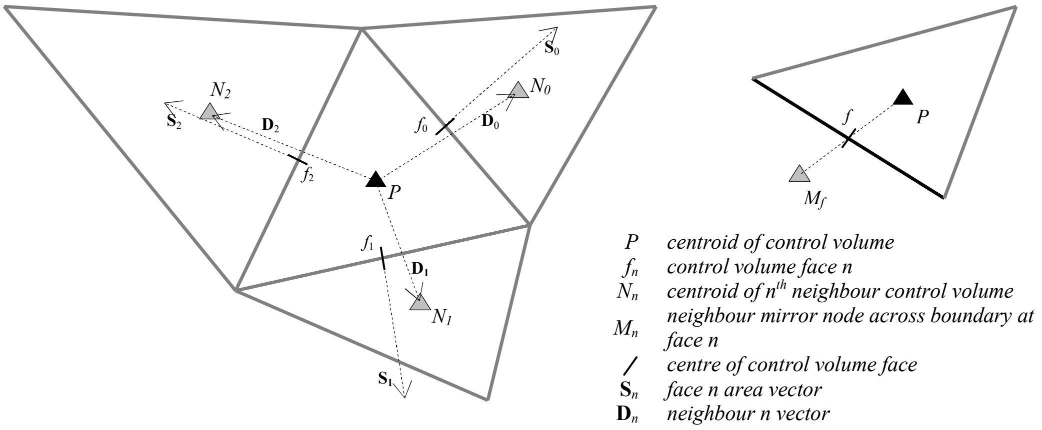

Figure 1. Control volume and neighbours, boundary mirror node configuration.

Considering the conservation of momentum in the x-direction (3a), integrating over the control volume surrounding computational node P gives:

$$\rho\int_V \frac{\partial u}{\partial t}\,dV = \mu\int_V \nabla\cdot\nabla u\,dV - \rho\int_V \nabla\cdot\left(\mathbf{U}u\right)dV - \int_V \nabla\cdot\left(p\mathbf{i}\right)dV \tag{4}$$

which, after simplification by the divergence theorem:

$$\rho\int_V \frac{\partial u}{\partial t}\,dV = \mu\int_S \nabla u\cdot d\mathbf{S} - \rho\int_S u\mathbf{U}\cdot d\mathbf{S} - \int_S p\mathbf{i}\cdot d\mathbf{S} \tag{5}$$

gives an expression describing the rate of change of x-momentum in terms of the convective and viscous fluxes through the control volume faces and the net pressure force acting on the volume. We consider now each term of the equation in turn.

– The ***time dependent term*** is discretised using a first order backward Euler scheme considering the velocity at P to be an average over the control volume:

$$\rho \int_V \frac{\partial u}{\partial t} dV = \rho V_P \left(\frac{\partial u}{\partial t} \right)_P = \rho V_P \left(\frac{u^{t+1} - u^t}{\Delta t} \right)_P \tag{6}$$

– The ***diffusion term*** is simplified using the midpoint rule to convert the surface integral to a discrete sum over the control volume faces. The diffusive flux through face f is then given by:

$$\mu\left((\nabla u)_f \cdot \mathbf{A}_f \right) = \mu A_f \left((\nabla u)_f \cdot \mathbf{n}_f \right) \tag{7}$$

where A_f is the face area and is equal to $|\mathbf{S}_f|$, and $\mathbf{n}_f = \frac{\mathbf{S}_f}{A_f}$ is the unit normal to the face f.

To take into account the non-orthongonality of the grid, the correction of Muzaferija[9] is applied:

$$(\nabla u)_f = \left(\overline{\nabla u}\right)_f + \left(\frac{u_N - u_P}{\left|\mathbf{D}_f\right|} - \left(\overline{\nabla u}\right)_f \cdot \mathbf{d}_f \right) \mathbf{d}_f \tag{8}$$

where $\left(\overline{\nabla u}\right)_f$ is a weighted average of the velocity gradients at the computational nodes either side of face f, and $\mathbf{d}_f = \frac{\mathbf{D}_f}{\left|\mathbf{D}_f\right|}$ is the unit vector between P and the neighbour on side f. The overbar denotes a value interpolated to the face from the control volume centre values either side. The calculation of velocity gradients at control volume centres, and their interpolation to control volume faces is described in section 2.5.

This gives the face diffusive flux, after substitution into (7) and manipulation, as:

$$\mu A_f \left((\nabla u)_f \cdot \mathbf{n}_f \right) = \mu A_f \left[\left(\frac{u_N - u_P}{\left|\mathbf{D}_f\right|} \right) \left(\mathbf{d}_f \cdot \mathbf{n}_f \right) + \left(\left(\overline{\nabla u}\right)_f - \left(\left(\overline{\nabla u}\right)_f \cdot \mathbf{d}_f \right) \mathbf{d}_f \right) \cdot \mathbf{n}_f \right] \tag{9}$$

The first term in the square brackets will be treated implicitly in terms of the unknown velocities at the cell centres. The second term is treated explicitly, and is zero when the grid is orthogonal.

– The ***convection term*** is also simplified using the midpoint rule, giving the convective flux through a control volume face as:

$$\rho u_f \left(\mathbf{U}_f \cdot \mathbf{S}_f \right) = \rho u_f A_f \left(\mathbf{U}_f \cdot \mathbf{n}_f \right) \tag{10}$$

The convection term is linearised by treating the mass flux through the face explicitly using current velocities:

$$m_f = \rho A_f \left(\mathbf{U}_f \cdot \mathbf{n}_f \right) \tag{11}$$

which gives the face convective flux as:

$$\rho u_f A_f \left(\mathbf{U}_f \cdot \mathbf{n}_f \right) = m_f u_f \tag{12}$$

wherein the interpolation needed to find the face mass flux is described in section 2.5.

– The ***pressure gradient term*** is also simplified using the midpoint rule; the contribution to the pressure term from face f is given by:

$$p_f \left(\mathbf{i} \cdot \mathbf{S}_f \right) = p_f A_f n_f^x \tag{13}$$

Thus the discretised x-momentum equation is:

$$\rho V_P \left(\frac{u^{t+1} - u^t}{\Delta t} \right)_P = \mu \sum_f A_f \left(\left(\frac{u_N - u_P}{\left| \mathbf{D}_f \right|} \right) \left(\mathbf{d}_f \cdot \mathbf{n}_f \right) + D_u^{\text{cross}} \right)_f - \sum_f m_f u_f - \sum_f p_f A_f n_f^x \tag{14}$$

where:

$$\left(D_u^{\text{cross}} \right)_f = \left(\left(\overline{\nabla u} \right)_f \cdot \mathbf{n}_f \right) - \left(\left(\overline{\nabla u} \right)_f \cdot \mathbf{d}_f \right) \left(\mathbf{n}_f \cdot \mathbf{d}_f \right) \tag{14a}$$

2.4 Implicit terms and differencing

The unknown face velocity in the convection terms (12) must be described in terms of the unknown nodal values at the centre of the control volumes either side of the face. A variety of schemes are available to compute this value, in this case the Power law scheme is implemented which uses Upwind differencing for the convected face velocity. Upwind differencing is known to introduce an artificial 'numerical' diffusion, so the Power law scheme compensates for this by reducing the influence of the fluid viscosity based on the local Peclet number of the face being considered, which is defined as:

$$Pe_f = \frac{m_f \left| \mathbf{D}_{PN} \right|}{\mu A_f \left(\mathbf{d}_f \cdot \mathbf{n}_f \right)} \tag{15}$$

where m_f is as defined in (11)

The discretised x-momentum equation is rearranged into the form:

$$a_P u_P = \sum_f a_N u_N + b_P \tag{16}$$

where the following definitions apply:

$$a_N = \frac{\mu A_f}{\left|\mathbf{D}_{PN}\right|}\left(\mathbf{d}_f \cdot \mathbf{n}_f\right) g\left(\left|Pe_f\right|\right) + \max\left(0, -m_f\right) \tag{16a}$$

$$a_P = \frac{\rho V_P}{\Delta t} + \sum_f \left(a_N + m_f\right) \tag{16b}$$

$$b_P = \frac{\rho V_P u_P^{t-1}}{\Delta t} + \mu \sum_f A_f D_u^{cross} - \sum_f p_f A_f n_f^x \tag{16c}$$

where $g\left(\left|Pe_f\right|\right) = \max\left(0, \left(1 - 0.1\left|Pe_f\right|\right)^5\right)$ where $\left|Pe_f\right|$ is the magnitude of the face Peclet number defined in (15).

2.5 Explicit terms and interpolation

Gradients of variables in the cross diffusion term (14a) are interpolated from centre gradient values found using the divergence theorem and are treated explicitly. At the control volume centre:

$$\left(\nabla u\right)_P = \frac{1}{V_P} \sum_f \overline{u}_f \mathbf{S}_f \tag{17}$$

where the overbar indicates that the face values $\overline{u}_f$ are found using a linear interpolation from the control volume central values either side of the face:

$$\overline{u}_f = \lambda_f u_N + \left(1 - \lambda_f\right) u_P \tag{18}$$

where $\lambda_f = \frac{\left|\mathbf{D}_{Pf}\right|}{\left|\mathbf{D}_{PN}\right|}$, the interpolation factor, is the ratio of the distances $\left|\mathbf{D}_{Pf}\right|$ from P to face f and $\left|\mathbf{D}_{PN}\right|$ from P to neighbour N. The error due to the angular difference in these two vectors is neglected. The same technique is then applied to the control volume centre velocity gradients found by (17) to interpolate for the face velocity gradients in (14a):

$$\left(\overline{\nabla u}\right)_f = \lambda_f \left(\nabla u\right)_N + \left(1 - \lambda_f\right)\left(\nabla u\right)_P \tag{19}$$

However, a different interpolation technique is required for the face mass fluxes used explicitly in the mass flux terms in (12), in order to avoid spurious oscillations in the pressure field which would not be felt by the momentum equations due to a lack of sufficient coupling of the equations. The approach of Rhie & Chow[10] is used here, wherein the face velocity found by interpolation using (18) is corrected to take into account a more direct interpolation of the pressure gradient:

$$u_f = \overline{\left[\frac{1}{a_P} \sum_f a_N u_N + \tilde{b}_P\right]_f} - \overline{\left[\frac{V_P}{a_P}\right]_f} \left(\left(\nabla p\right)_f \cdot \mathbf{i}\right) \tag{20}$$

where $\widetilde{b}_P$ is the *x*- momentum source term not including pressure gradient, a_P is the central coefficient of the discretised momentum equation as defined in (16b), and the overbar again denotes interpolation to the face using the control volume centre values either side.

Equation (20) can be shown is equivalent to:

$$u_f = \overline{u}_f + \overline{\left[\frac{V_P}{a_P}\right]}_f \left[\overline{\left((\nabla p)_P \cdot \mathbf{i}\right)}_f - \left((\nabla p)\cdot \mathbf{i}\right)_f\right] \tag{21}$$

Now computing the face mass flux required:

$$m_f = \rho A_f\left(\mathbf{U}_f \cdot \mathbf{n}_f\right) = \rho A_f\left(\overline{\mathbf{U}}_f \cdot \mathbf{n}_f\right) + \rho A_f \overline{\left[\frac{V_p}{a_P}\right]}_f \left[\left(\overline{\left((\nabla p)_P\right)}_f - (\nabla p)_f\right)\cdot \mathbf{n}_f\right] \tag{22}$$

where:

$$\overline{\left((\nabla p)_P\right)}_f = \lambda(\nabla p)_N + (1-\lambda)(\nabla p)_P \tag{22a}$$

$$(\nabla p)_f = \left(\frac{p_N - p_p}{\left|\mathbf{D}_{PN}\right|}\right)\mathbf{d}_{PN} \tag{22b}$$

2.6 Solution for pressure

The SIMPLE algorithm of Patankar and Spalding[11] is used to introduce a pressure correction equation using the equation of conservation of mass (continuity equation) (2). The velocities found from solution of the momentum equation (14) will in general, during the solution procedure, not satisfy continuity of mass since the divergence-free condition is not implied in the momentum equations and the pressure field used in their calculation is treated explicitly.

If the velocities and pressures are considered to be made up of an initial guess and a correction, the discretised continuity equation (2) becomes:

$$a_{Pp'}p'_P = \sum_N a_{Np'}p'_N + b_{Pp'} \tag{23}$$

where p' is the pressure correction required, and the following coefficients apply:

$$a_{Np'} = A_f \overline{\left[\frac{V_P}{a_P}\right]}_f \left(\frac{\mathbf{d}_{PN}\cdot \mathbf{n}_f}{\left|\mathbf{D}_{NP}\right|}\right) \tag{23a}$$

$$a_{Pp'} = \sum_N a_{Np'} \tag{23b}$$

$$b_{Pp'} = -\sum_f A_f\left(\overline{\mathbf{U}^*_f} \cdot \mathbf{n}_f\right) \tag{23c}$$

Considering the definition of face mass fluxes, the pressure correction source term (23c) can be considered as:

$$b_{Pp'} = -\frac{1}{\rho}\sum_f \overline{m_f^*} \tag{24}$$

Since the mass fluxes in (24) are evaluated using interpolated velocities, the Rhie-Chow correction described in section 2.5 is also used here.

Once (23) has been solved for the pressure corrections, the velocity corrections are calculated by:

$$u'_P = -\frac{V_P}{a_P}\left((\nabla p')_P \cdot \mathbf{i}\right) \tag{25}$$

wherein the method described in section 2.5 is used for the evaluation of pressure correction gradients. The velocities and pressure are then corrected according to:

$$\mathbf{U}_P = \mathbf{U}_P^* + \mathbf{U}'_P \tag{26a}$$

$$p_p = p_P^* + p'_P \tag{26b}$$

where the star indicates a ‘guessed’ variable, in this case the velocity found after solution of the momentum equations, and the pressure used for that solution.

2.7 Relaxation

An iterative approach to the solution of the momentum equations (14) is adopted. To aid stability the velocities are over-relaxed. Considering (16):

$$u_P^{t+1} = (1-\alpha_{vel})u_P^t + \alpha_{vel}\left[\frac{\sum\limits_N a_N u_N + b_P}{a_P}\right] \tag{27}$$

where α_{vel} is the velocity over-relaxation factor, chosen between 0 and 1, which effectively finds the new velocity as a blend of the velocity at the previous timestep and the velocity calculated by (16). The same factor is used for both *x*- and *y*- momentum calculations.

The velocity relaxation is duly taken into account in the calculation of the explicit Rhie-Chow mass fluxes as described in section 2.5 where (22) becomes:

$$m_f = \rho A_f\left(\mathbf{U}_f \cdot \mathbf{n}_f\right) = \rho A_f\left(\overline{\mathbf{U}}_f \cdot \mathbf{n}_f\right) + \rho A_f \alpha_{vel}\overline{\left[\frac{V_p}{a_P}\right]}_f \left[\left(\overline{\left((\nabla p)_P\right)}_f - (\nabla p)_f\right)\cdot \mathbf{n}_f\right] \tag{28}$$

and in the calculation of the velocity corrections where (25) becomes:

$$u'_P = -\alpha_{vel}\frac{V_P}{a_p}\left(\frac{\partial p'}{\partial x}\right)_P \tag{29}$$

The correction to the pressure is under-relaxed to compensate for the simplifying assumptions made in the formulation of the pressure correction equation. (26b) becomes:

$$p_P = p_P^* + \alpha_p p'_P \tag{30}$$

where α_p is the pressure under-relaxation factor which damps the rate of change of the pressure field.

2.8 Implementation of boundary conditions

Conditions on velocities and pressure at the boundaries of the domain are imposed through the use of 'mirror nodes'. The value of the variable at the mirror node is set so that interpolations to the face of the volume on the boundary produce the required condition. The boundary node is located such that the vector *PN* on that side passes through the centre of the boundary face in order to maximise the accuracy of the midpoint rule approximations. The non-orthoganlities are taken into account in the same manner as for internal volume faces. The mirror node arrangement is shown in Figure 1.

2.9 Algorithm structure

An iterative approach to the solution of both the momentum equations and the pressure correction equations is taken. The convergence is judged by considering the rate of change of update on the variables from one iteration of the momentum and pressure correction equations to the next. The tolerance is set at 0.1% of the total update in each control volume, averaged over the whole mesh.

Calculations to a steady state are carried out using the time-dependent term to aid stability of the iterative solution, with the explicit time dependent source term being updated at the end of every iteration. Time dependent unsteady calculations are formulated by driving each timestep to the convergence tolerance, and then advancing to the next timestep. In this case the time dependent source term is held constant from one iteration to the next, and is updated at the beginning of each timestep.

2.10 Formulation on a moving mesh

A boundary fitted deforming mesh is used in this project. The motion of the fluid-structure boundary causes motion of all mesh nodes so that the mesh adapts and remains fitted to the boundary. This approach ensures that the topology of the mesh remains constant throughout the simulation, and so neighbour finding routines, which are computationally expensive on unstructured meshes, are only carried out once at the beginning of the algorithm. Furthermore, re-meshing of the domain is avoided, which is also computationally expensive and can introduce errors during the interpolation of the flow field from one mesh to the next. The motion of the mesh nodes could also be related to the fluid solution in order to cause the mesh to adapt and cluster nodes in areas of interest such as regions of high vorticity. Models for controlling mesh deformation will be discussed in section 4. Thus the control volumes used for the discretisation of the equations of motion are moving and deforming over time.

2.10.1 Equations of motion on a moving mesh

The differential equations of motion (1) and (2) can be integrated over a control volume whose bounding surface moves with time. An additional equation, known as the geometric conservation law, must be considered[12]:

$$\frac{d}{dt}\int_V dV - \int_V \nabla \cdot \mathbf{V}_S dV = 0 \tag{31}$$

where $\mathbf{V}_S$ is the velocity of the control volume surface.

Equation (31) states that any change of the volume of the fluid mesh element must be equal to the volume swept by its bounding surface. For an incompressible fluid, and considering (31), the continuity equation (2) remains unchanged on a moving mesh[13]. In the formulation of the momentum equation, however, the motion of the boundary must be taken into account when calculating the face mass fluxes in the convection term. The integral equations of conservation of *x*-momentum, after simplification by the divergence theorem as previously described, now are:

$$\rho \frac{d}{dt}\int_V u dV = \mu \int_S \nabla u \cdot d\mathbf{S} - \rho \int_S u(\mathbf{U} - \mathbf{V}_S)\cdot d\mathbf{S} - \int_S p\mathbf{i} \cdot d\mathbf{S} \tag{32}$$

The time-dependent term is discretised according to:

$$\rho \frac{d}{dt}\int_V u dV = \rho \left(\frac{u^{t+1}V^{t+1} - u^t V^t}{\Delta t} \right)_P \tag{33}$$

The momentum equations are discretised as described in section 2.3, except that the net face mass flux is calculated for the convective term taking into account the mesh velocity:

$$m_f = \rho A_f (\mathbf{U} - \mathbf{V}_S)_f \cdot \mathbf{n}_f \tag{34}$$

As the continuity equation remains independent of the mesh motion, so the pressure correction procedure is also unchanged in comparison with the formulation on a stationary mesh.

3 RESULTS

3.1 Simulations on a stationary mesh

3.1.1 Flow past a normal flat plate

This case was chosen to test the ability of the approach to model a zero thickness boundary enclosed in the domain. Large pressure differences occur across the internal boundary, and the flow behind the plate is strongly rotational. The steady case was modelled where the pair of vortices formed behind the plate remains attached to the plate. The Reynolds number is defined with respect to the plate height, and a selection of cases in the range *Re* = 1.2 – 18 were studied. The length of the recirculating vortices, as shown in Figure 3, non-dimensionalised with respect to the plate height, and the drag forces felt by the plate were compared to available data. The drag coefficient is defined as:

$$C_D = \frac{2F^x}{\rho u_{\max}^2} \tag{35}$$

where F^x is the net force on the cylinder in the x-direction. Due to its zero thickness, the flat plate experiences only pressure drag (or form drag) induced by the pressure difference between its two sides. The geometry of the domain and the parameters of the wake are shown in Figure 3.

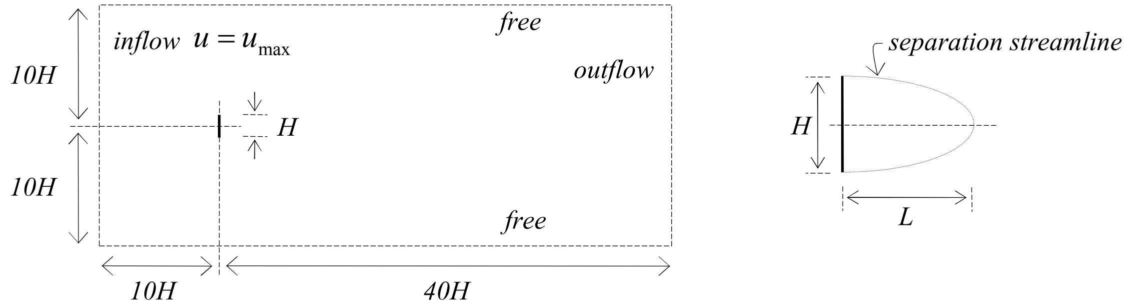

Figure 3. Flow past a normal flat plate: domain geometry and steady wake parameters.

Simulations were carried out on two different meshes having 24 or 48 elements on each face of the plate, which had 16,038 and 19,872 elements in total. The meshes were refined in the area around the tips of the plate and in the wake by placing extra mesh edges there in the mesh generating process. The velocity over-relaxation factor was 0.8, the under-relaxation factor on pressure update was 0.02 and the non-dimensional timestep was 0.25. The initial conditions were zero pressure and maximum oncoming velocity at all internal nodes. The no-slip condition was imposed on the mesh edges coincident with the plate.

Figure 4 shows the variation of non-dimensionalised eddy length with Reynolds number, in comparison with published data; the results demonstrate a clear agreement, particularly with the work of Hudson & Dennis[14] and Dennis *et al*[15] who use a finite difference approach on a polar grid, in primitive variable and stream function-vorticity formulation respectively.

The variation of drag coefficient with Reynolds number is shown in Figure 5, also demonstrating good agreement with published data.

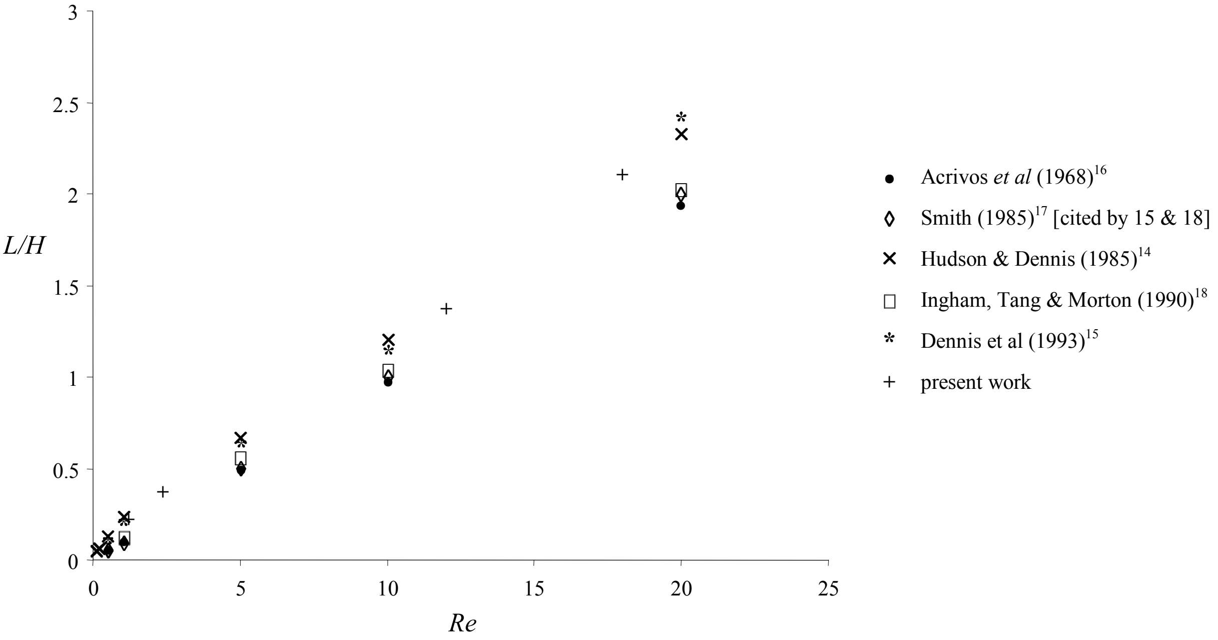

Figure 4. Flow past a normal flat plate: variation of non-dimensionalised eddy length with Reynolds number.

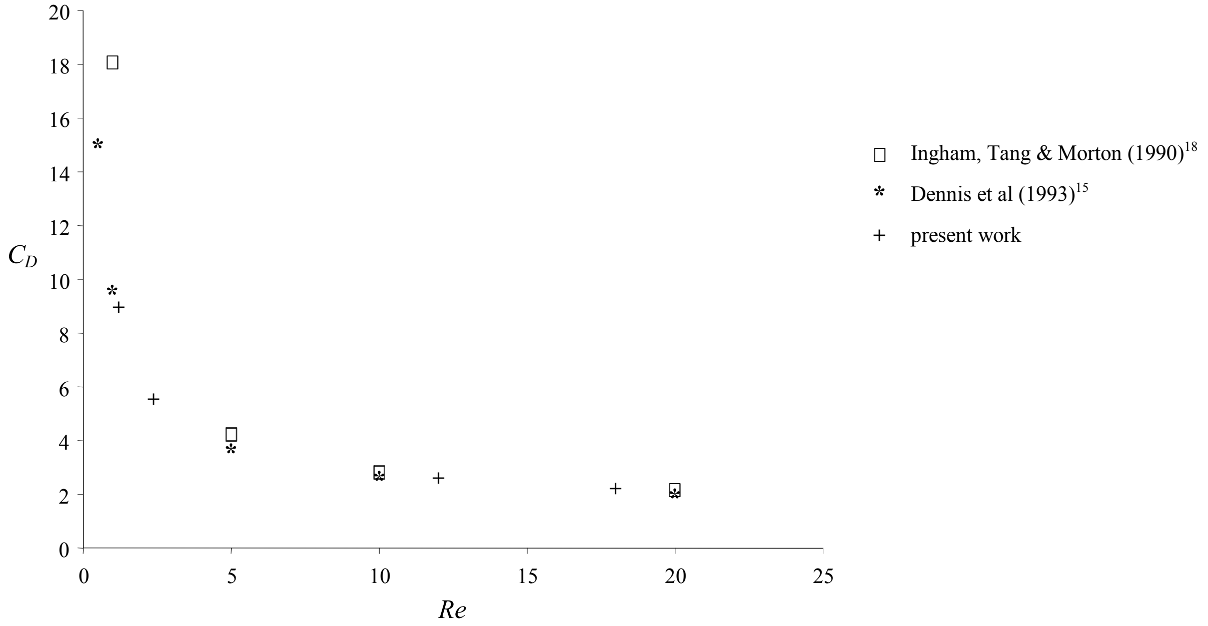

Figure 5. Flow past a normal flat plate: variation of drag coefficient with Reynolds number.

3.1.2 Flow past a cylinder

The previous test case exhibits separation of the flow at well defined points; in this case the point of separation is not known *a priori*, and therefore the ability of the model to predict separation from a smooth surface will be demonstrated.

The Reynolds number of the flow is defined using the diameter of the cylinder as the characteristic length scale. The geometry of the computational domain and the wake parameters are shown in Figure 6. In the following cases the initial conditions were zero pressure and maximum oncoming velocity at all internal nodes. The no-slip condition was imposed on the mesh edges coincident with the cylinder.

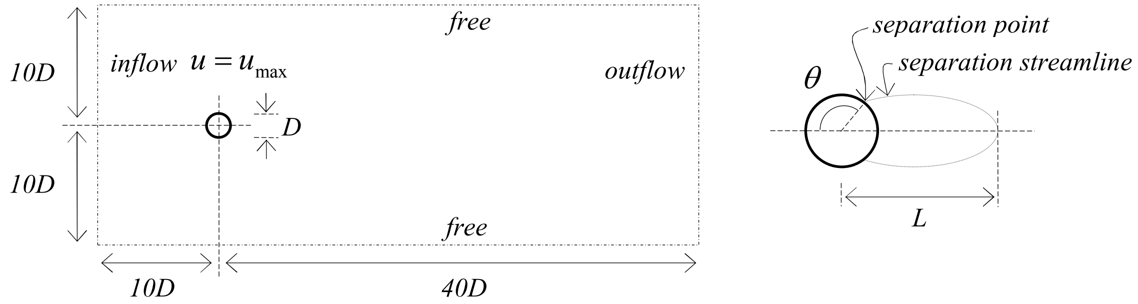

Figure 6. Flow past a cylinder: domain geometry and steady wake parameters.

3.1.2.1 *Re* = 40, steady and unsteady formulation

The simulations were carried out on three meshes, having 80, 120 and 180 elements around the cylinder, having a total of 24,098, 38,270 and 144,228 elements respectively. A non-dimensional timestep of 0.25s was used in all cases. The initial conditions are zero pressure and maximum oncoming velocity at all internal nodes. The over-relaxation factor on velocities was 0.8 and the under-relaxation factor on pressure update was 0.02. A detail of the coarsest mesh is shown in Figure 7. The mesh has been refined in the area around the cylinder and in the wake as shown.

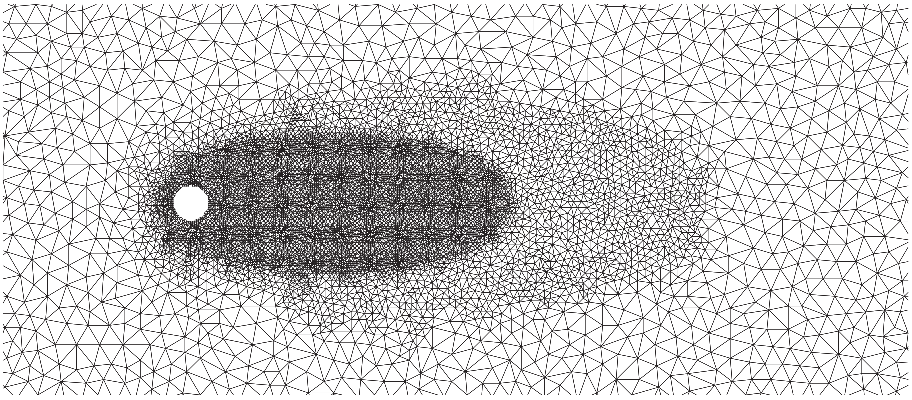

Figure 7. Detail of mesh refinement around the cylinder and in the wake.

The non-dimensionalised eddy length (*L/D*) and the separation angle θ, as defined in Figure 6, are used for comparison with published results. The pressure and drag coefficients are also considered. The pressure coefficient at a point on the cylinder surface is defined as:

$$C_P = \frac{2(p - p_0)}{\rho u_{\max}^2} \tag{36}$$

where p_0 is the uniform pressure far from the cylinder, in this case zero, and $u_{\max}$ is the oncoming flow velocity.

The drag coefficient is as defined in Equation (35), where F^x in this case is the net force on the cylinder in the *x*-direction, as a result both of pressure differences around the cylinder and viscous stresses at the cylinder surface. The viscous force is evaluated by applying an equal and opposite viscous force on the cylinder to that which the cylinder applies in the evaluation of the momentum of the elements of fluid in contact with its surface. The pressure force is evaluated by integrating the pressure around the cylinder. The drag due to pressure is approximately twice the drag due to friction for this case.

Table 1 provides a comparison of the results on the finest mesh with a selection of available literature for this case. The results for the two coarser meshes were also good, remaining within a 4% range of the results on the finest mesh.

	eddy length 2L/D	C_D	C_p **front**	C_p **rear**	θ^o
Son & Hanratty (1969)[19]	6	1.6	-	-	126.1
Dennis & Chang (1970)[20]	5.69	1.522	1.144	-0.509	126.2
Collins & Dennis(1973)[21]	5.3	1.56	1.16	-0.53	126.4
Coutanceau & Bouard(1977)[22]	5.26	-	-	-	126.5
Borthwick (1986)[23]	-	1.507	-	-	126.3
Franke, Rodi & Schonung (1990)[24]	5.72	1.52	1.15	-0.5	126.2
Koumoutsakos & Leonard(1995)[25]	-	1.69	-	-	128
Present work (steady formulation)	5.38	1.614	1.186	-0.520	127.8
Present work (unsteady formulation)	5.35	1.615	1.184	-0.529	127.9

Table 1. Parameters of flow past a cylinder, $Re = 40$.

3.1.2.2 *Re* = 100, unsteady formulation

Flow at this Reynolds number produces unsteady behaviour, characterised by the onset of oscillation of the attached vortices, which increases in magnitude until they are eventually alternately shed into the stream forming the familiar Von Karman vortex street in the wake. This case was used to test the ability of the formulation to model time-varying behaviour, and vortex shedding in particular.

Initial simulations were carried out on the coarsest mesh described in section 3.4.1 since the results on this mesh for the $Re = 40$ case agreed well with published data and thus investigation into the optimum combination of relaxation parameters could be achieved more rapidly. A non-dimensional timestep of 0.01 was used, in combination with a velocity over-relaxation factor of 0.8 and a pressure under-relaxation factor 0.05.

The lift coefficient is defined in a similar manner to the drag coefficient (35) considering the net force on the cylinder in the *y*-direction. A snapshot of the velocity vector field at *t*=100 is shown in Figure 8, and the variation with time of the drag and lift coefficient of the cylinder are shown in Figure 9. Time is non-dimensionalised with respect to the cylinder diameter and the oncoming flow *x*-direction velocity component.

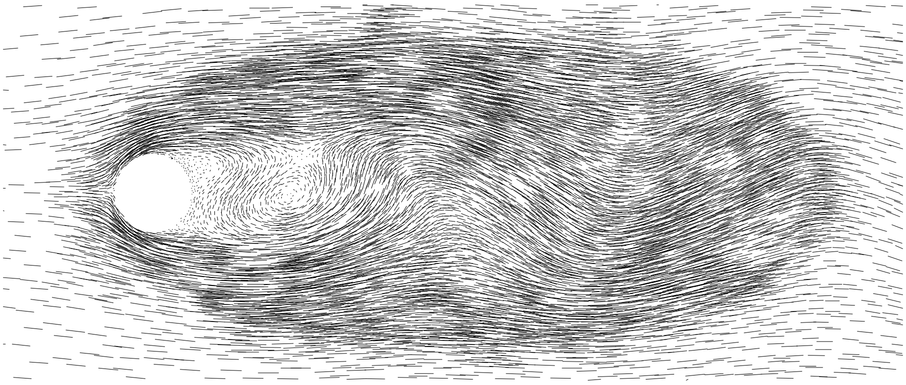

Figure 8. Flow past a cylinder, *Re* = 100: velocity vectors at non-dimensionalised *t* = 100.

Figure 8 shows the shedding of vortices from the cylinder into the wake, and Figure 9 shows the accompanying oscillations in the drag and lift forces on the cylinder. The drag coefficient has stabilised to a value of 1.4±0.005 and the lift coefficient to ±0.24. Zhou & Graham[26] cite a range of drag coefficients for this case of 1.29-1.82, whilst Borthwick[23] finds a drag coefficient of 1.215± 0.01 and a lift coefficient of ±0.26.

The Strouhal number of shedding is defined as:

$$St = \frac{fD}{u_{\max}} \tag{37}$$

where f is the frequency of shedding D is the diameter of the cylinder and $u_{\max}$ is the oncoming flow velocity in the x-direction. By considering the oscillations in the lift coefficient, it can be seen that the Strouhal number here is 0.154, which lies within the range 0.152-0.174 cited by Zhou & Graham[26].

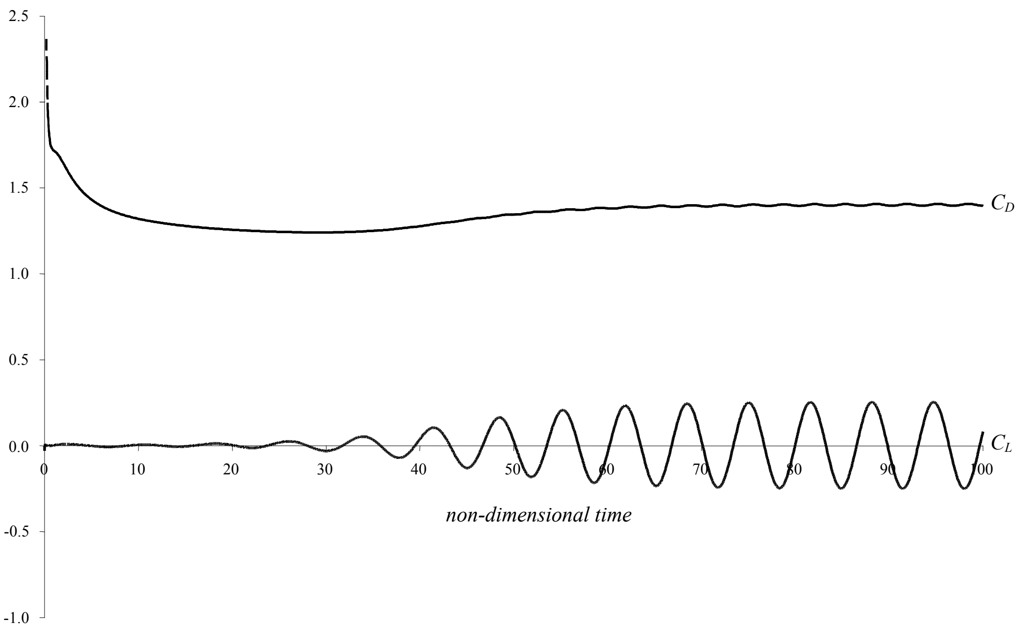

Figure 9. Flow past a cylinder, Re = 100: development of drag and lift coefficient with time.

3.2 Simulations on a moving mesh

An arbitrary mesh motion is imposed during the steady solution in order to test the formulation described in section 2.10.1. The mesh motion is generated by superimposing a random time-varying perturbation on all internal mesh nodes. Mesh tangling is avoided by setting the magnitude of the perturbation to be a fixed fraction of the smallest mesh link length; the direction of the perturbation is then decided randomly at each location. In this case the magnitude of perturbation was 30% of the smallest mesh edge length. Over time, no net translation of the control volumes occurs, and the movement can be thought of as a vibration of the mesh edges causing distortion of the control volumes. This is a harsh mesh motion test, since the motion of any one mesh edge is completely independent of the motion of the edges around it, and is independent from one iteration or timestep to the next.

3.2.1 Flow past a normal flat plate

This test case was carried out on a stationary mesh to validate the model against existing data as reported in section 3.1.1, and then on an arbitrarily moving mesh to test the formulation described in section 2.10.1. The Reynolds number 18 flow is modelled with the same initial and boundary conditions, relaxation parameters and timestep as the stationary mesh case described in section 3.1.1. Both steady and unsteady formulation were used; in the steady formulation, the mesh motion is imposed each iteration, in the unsteady formulation, the nodes are moved at the beginning of each timestep.

Figure 10 shows a detail of the mesh near the plate and the velocity vectors of the steady state, calculated on a stationary mesh. Figure 11 shows the same figures for the case on the moving mesh. In both velocity vector plots the plate is omitted for clarity. As shown, the velocity field on the moving mesh agrees well with that on the stationary mesh.

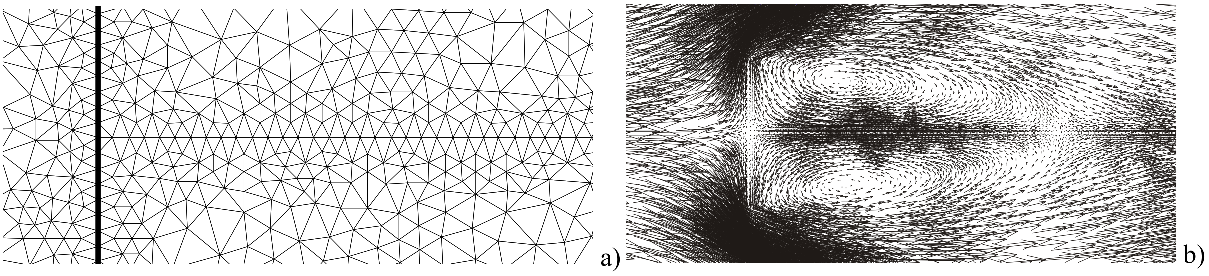

Figure 10. Flow past a normal flat plate, *Re* = 18, stationary mesh: a) mesh detail, b) velocity vectors.

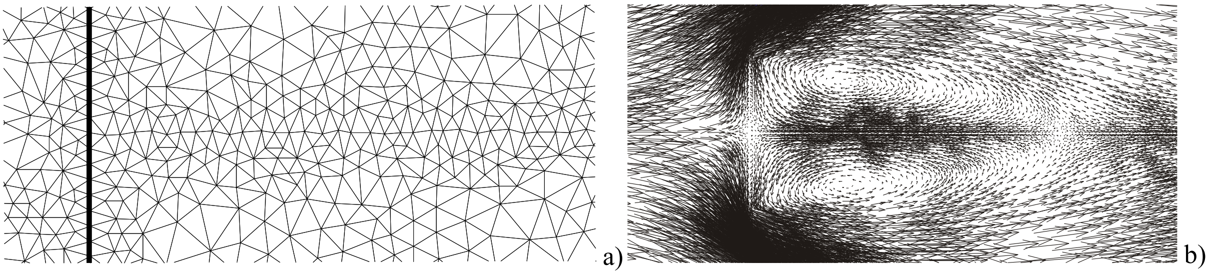

Figure 11. Flow past a normal flat plate, *Re* = 18, arbitrarily moving mesh: a) mesh detail, b) velocity vectors.

The drag coefficient, as defined by equation (35) is also monitored, and is shown in Figure 12 for both the steady and unsteady formulations on both the stationary and arbitrarily moving mesh. Good agreement is again demonstrated between the steady and unsteady formulations, and between the stationary and moving mesh cases.

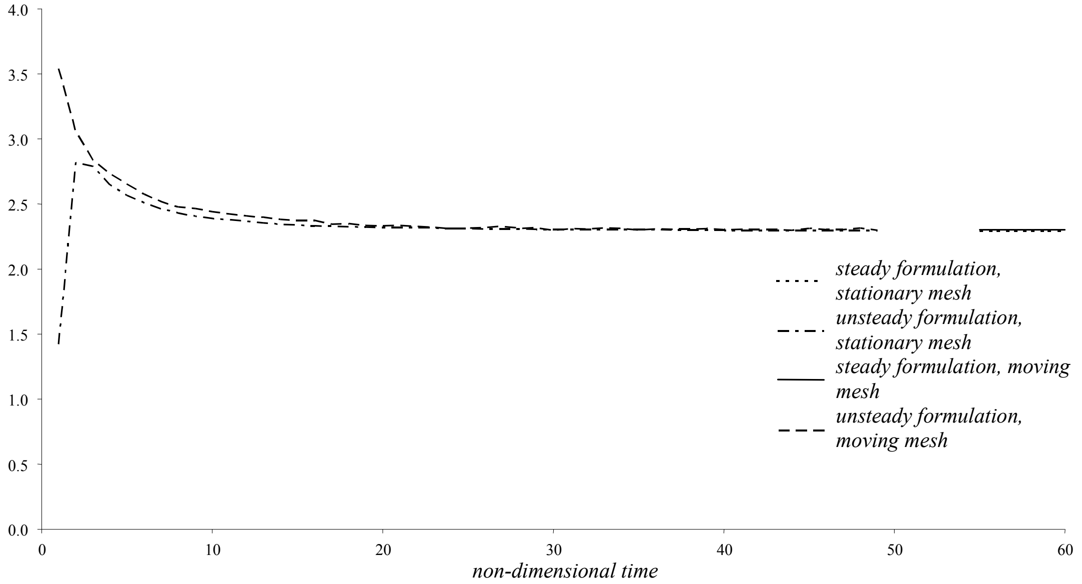

Figure 12. Flow past a normal flat plate, *Re* = 18, stationary and moving meshes: evolution of drag coefficient.

3.2.2 An alternative formulation

The integration of the momentum equation on a moving mesh can alternatively be described as follows, by considering the change in velocity following the moving control volume centroid:

$$\left(\frac{\delta u}{\delta t}\right)_P = \frac{1}{\int_V dV}\left(\mu\int_S \nabla u \cdot d\mathbf{S} - \rho\int_S u\mathbf{U}\cdot d\mathbf{S} - \int_S p\mathbf{i}\cdot d\mathbf{S}\right) + \left(\mathbf{V}_P \cdot \nabla u\right)_P \tag{38}$$

where $\mathbf{V}_P$ is the velocity of the centroid P of the moving control volume. We aim to investigate the differences between the two approaches described here in the near future.

4 FLUID-STRUCTURE COUPLING

To model the interactions of fluid flow with a flexible structural membrane the proposed approach will couple a flexible 1-D poly-linear structure, with the 2-D unstructured fluid model presented in this paper. The loads on the structure will be determined from fluid forces due to the imposed boundary conditions at the fluid-structure interface. The motion of the structure will then be determined following the dynamic relaxation technique of Day[27] applied to tensile structures following the approach of Barnes[28]. The structure is considered as a dynamic system of elements, and its motion is traced over time until equilibrium is reached. The main advantage of this approach is its ability to model easily large deformations of the structure, and non-linear material characteristics.

The motion of the flexible structure will in turn induce motion of the body-fitted mesh. The mesh motion must be carefully controlled in order to maintain grid quality at all times throughout the mesh and to avoid the creation of inverted elements. A good quality mesh is one in which adjacent control volumes do not vary too greatly or rapidly in size, which can be achieved by assigning a volumetric-type stiffness to the mesh elements, which varies inversely with element size, leading to smaller elements moving more as a rigid body, and larger elements distorting more than displacing. Furthermore, ensuring that triangle aspect ratios do not become too large will control mesh distortion and therefore also limit non-orthogonality. Simple algebraic mesh motion models are not appropriate here due to the complexity of the structure deformations; in this project a pseudo-structure approach will be taken. The mesh motion will be calculated using the same method as the structure motion, considering the system as a combination of discrete structural elements. This approach is similar, for example, to the lineal-spring analogy of Batina as implemented by Robinson, Batina and Yang[29] or the torsional spring model of Degand & Farhat[30]. In this way, the structure and mesh will be considered as one dynamic system, with applied loads and accurate material properties only at the ‘real’ structure elements, and varying stiffness parameters at the mesh ‘pseudo’ structure elements in order to control grid quality.

5 CONCLUSIONS

The current algorithm has been shown to reliably predict a number of fluid flow phenomena including separation from corners and smooth surfaces, and vortex shedding on unstructured non-orthogonal grids. Good agreement with published experimental and numerical data was demonstrated for the steady case of flow past a normal flat plate at *Re* in the range 1.2-18 and for the case of non-shedding flow past a cylinder at *Re*=40, the latter case also showed good agreement between the steady and unsteady formulations. The unsteady case of flow past a cylinder at *Re*=100 demonstrated vortex shedding at a frequency in agreement with published data, even on the coarsest mesh used for the steady *Re*=40 case. No discernible difference was found between the simulations on a stationary mesh and on a mesh having a super-imposed arbitrary vibration in the steady case of flow past a normal flat plate at Re=18. This case is an encouraging initial test for the formulation on a moving mesh.

Further development will extend the approach to consider the interactive behaviour of the flow with a flexible internal boundary. The extension of this approach to three dimensions would be straightforward using an unstructured tetrahedral fluid mesh and a triangulated mesh of straight links for the membrane structure.

REFERENCES

[1] P.S. Jackson and G. W. Christie, “Numerical analysis of three-dimensional elastic membrane wings”, *AIAA Journal*, **25**, 676-682 (1987).

[2] P.S. Jackson and S.P. Fiddes, “Two-dimensional viscous flow past flexible sail sections close to ideal incidence”, *The Aeronautical Journal*, **99**, 217-225 (1995).

[3] W. Shyy and R. Smith, “Computation of laminar flow and flexible structure interaction”, *Computational Fluid Dynamics Review 1995*, Hafez & Oshima (eds), John Wiley & Sons (1995).

[4] R. Smith and W. Shyy, “Computation of aerodynamic coefficients for a flexible membrane airfoil in turbulent flow: A comparison with classical theory”, *Phys. Fluids*, **8**, 3345-3353 (1996).

[5] D.J.J Farnell, T. David and D.C. Barton, “Coupled states of flapping flags”, *Journal of Fluids and Structures*, **19**, 29-36 (2004).

[6] K.R. Stein, T.E. Tezduyar, V. Kumar, S.V. Sathe, R.J. Benney and R.D. Charles “Numerical simulation of soft landing for clusters of cargo parachutes”, *Proceedings of ECCOMAS 2004*, Neittaanmäki, Rossi, Korotov, Oñate, Périaux and Knörzer (eds) (2004).

[7] T. Tezduyar and Y. Osawa, “Fluid-structure interactions of a parachute crossing the far wake of an aircraft”, *Comput. Methods Appl. Mech. Engrg.*, **191**, 717-726.

[8] ‘Triangle’, Jonathan Schewuck, http://www.cs.cmu.edu/~quake/triangle.html

[9] S. Muzaferija, “Adaptive finite volume method for flow predictions using unstructured meshes and multigrid approach”, PhD Thesis, Univeristy of London (1995).

[10] C.M. Rhie and W.L. Chow, “Numerical study of the turbulent flow past an airfoil with trailing edge separation”, *AIAA Journal*, **21**, 1525-1532 (1983).

[11] S.V. Patankar and D.B. Spalding, "A calculation procedure for heat, mass and momentum transfer in three-dimensional parabolic flows", *Int. J. Heat Mass Transfer*, **15**, 1787-1806 (1972).

[12] P.D. Thomas and C.K. Lombard, "Geometric conservation law and its application to flow computations on moving grids", *AIAA Journal*, **17**, 1030-1037 (1979).

[13] J.H. Ferziger and M. Peric, *Computational Methods for Fluid Dynamics*, Springer, 3rd Edition, (2002).

[14] J.D. Hudson and S.C.R. Dennis, "The flow of a viscous incompressible fluid past a normal flat plate at low and intermediate Reynolds numbers: the wake", *J. Fluid Mech.*, **160**, 369-383 (1985).

[15] S.C.R. Dennis, W. Qiang, M Coutanceau and J-L. Launay, "Viscous flow normal to a flat plate at moderate Reynolds numbers"' *J. Fluid Mech.*, **248**, 605-635 (1993).

[16] A. Acrivos, L.G. Leal, D.D. Snowden and F. Pan, "Further experiments on steady separated flows past bluff objects", *J. Fluid Mech.*, **34**, 25-48 (1968).

[17] F.T. Smith, "On large-scale eddy closure", *J. Math. Phys. Sci.*, **19**, 1- (1985).

[18] D.B. Ingham, T. Tang and B.R. Morton, "Steady two-dimensional flow through a row of normal flat plates", *J. Fluid Mech.*, **210**, 281-302 (1990).

[19] J.S. Son and T.J. Hanratty, "Numerical solution for the flow around a cylinder at Reynolds numbers of 40,200 and 500", *J. Fluid Mech.*, **35**, 369-386 (1969).

[20] S.C.R. Dennis and G-Z. Chang, "Numerical solutions for steady flow past a circular cylinder atReynolds numbers up to 100", *J. Fluid Mech.*, **42**, 471-489 (1970).

[21] W.M. Collins and S.C.R. Dennis, "Flow past an impulsively started circular cylinder", *J. Fluid Mech.* **60**, 105-127 (1973).

[22] M. Coutanceau and R. Bouard, "Experimental determination of the main features of the viscous flow in the wake of a circular cylinder in uniform translation. Part 1. Steady flow", *J. Fluid Mech.*, **79**, 231-256 (1977).

[23] A. Borthwick, "Comparison between two finite-difference schemes for computing the flow around a cylinder", *Internat. J. Numer. Methods Fluids*, **6**, 275-290 (1986).

[24] R. Franke, W. Rodi & B. Schönung, "Numerical calculation of laminar vortex-shedding flow past cylinders", *Journal of Wind Engineering and Industrial Aerodynamics*, **35**, 237-257 (1990).

[25] P. Koumoutsakos and A. Leonard, "High-resolution simulations of the flow around an impulsively started cylinder using vortex methods", *J. Fluid Mech.*, **296**, 1-38 (1995).

[26] C.Y. Zhou and J.M.R. Graham, "A numerical study of cylinders in waves and currents", *Journal of Fluids and Structures*, **14**, 403-428 (2000).

[27] A.S. Day, "An introduction to dynamic relaxation", *The Engineer*, **219**, 218-221 (1965).

[28] M.R. Barnes, "Form finding and analysis of tension structures by dynamic relaxation", *International Journal of Space Structures*, **14**, 89-104 (1999).

[29] B.A. Robinson, J.T. Batina and H.T.Y. Yang, "Aeroelastic analysis of wings using the Euler equations with a deforming mesh", *J. Aircraft*, **28**, 781-788 (1991).

[30] C. Degand and C. Farhat, "A three-dimensional torsional spring analogy method for unstructured dynamic meshes", *Comput. & Structures*, **80**, 305-316 (2002).